Soft Matter

PAPER

View Article Online
View Journal | View Issue

Cite this: *Soft Matter*, 2022, **18**, 1089

Magnetic response of $CoFe_2O_4$ nanoparticles confined in a PNIPAM microgel network†

Marcus U. Witt, [a] Joachim Landers, [b] Stephan Hinrichs, [c] Soma Salamon, [b] Juri Kopp, [b] Birgit Hankiewicz, [c] Heiko Wende [b] and Regine von Klitzing *[a]

Received 8th November 2021,
Accepted 23rd December 2021

DOI: 10.1039/d1sm01597d

rsc.li/soft-matter-journal

The paper addresses coupling of magnetic nanoparticles (MNPs) with the polymer matrix of temperature-sensitive microgels and their response to magnetic fields. Therefore, $CoFe_2O_4$@CA (CA = citric acid) NPs are embedded within *N*-isopropylacrylamid (NIPAM) based microgels. The volume phase transition (VPT) of the magnetic microgels and the respective pure microgels is studied by dynamic light scattering and electrophoretic mobility measurements. The interaction between MNPs and microgel network is studied *via* magnetometry and AC-susceptometry using a superconducting quantum interference device (SQUID). The data show a significant change of the magnetic properties by crossing the VPT temperature (VPTT). The change is related to the increased confinement of the MNP due to the shrinking of the microgels. Modifying the microgel with hydrophobic allyl mercaptan (AM) affects the swelling ability and the magnetic response, *i.e.* the coupling of MNPs with the polymer matrix. Modeling the AC-susceptibility data results in an effective size distribution. This distribution represents the varying degree of constraint in MNP rotation and motion by the microgel network. These findings help to understand the interaction between MNPs and the microgel matrix to design multi responsive systems with tunable particle matrix coupling strength for future applications.

1 Introduction

Polymer gels are used for tissue engineering[1], drug delivery[2] or sensors.[3] The cross-linking is realized in different ways, for example by metal ions[4] or covalently bound cross-linker molecules. This study uses the monomer *N*-isopropylacrylamide (NIPAM) and the cross-linker *N*,*N*′-methylene-bis(acrylamide) (BIS). NIPAM and the resulting polymer (PNIPAM) show a lower critical solution temperature (LCST) at 32 °C in water.[5,6] When heating the gel above the volume phase transition temperature (VPTT) water becomes a poor solvent and is expelled from the gel.[7–11] Gels can be classified by their size *e.g.* macrogels or microgels. Microgels are smaller than 1 mm and offer the benefit of short response times to external stimuli. The temperature gradient inside the microgel is much smaller compared to the respective macrogel[12] if an external temperature change is applied. Surface coatings are realized easier with microgel, instead of growing the macrogel directly onto the surface. These benefits open up many applications for actuators or sensors. Such sensors are sensitive to temperature,[13] pH[14] or bio molecules such as glucose[15] or streptavidin.[16]

Doping microgels with metallic nanoparticles (NPs) allows a response of the gels to external field like light or magnetic fields. For example gold NPs are used as local hot spots in thermoresponsive PNIPAM microgels. They transform light energy into heat *via* plasmon coupling.[17] By heating (and shrinking) PNIPAM microgels the embedded gold NPs change their optical properties.[18] Microgels that are doped with magnetic nanoparticles (MNPs) react to external magnetic fields,[19] while the MNPs may also act as local hot spots in alternating magnetic fields (hyperthermia). The resulting magnetic microgels (MMgs) may also respond to static external magnetic fields by deformation of the polymer matrix.[20] Magnetic poly(*N*-vinylcaprolactam)/glycidyl methacrylate gels are self assembling.[21] Many studies focus on core/shell structures of magnetic cores and a polymer shells[22–26] or polymer core and magnetic shell.[27,28] Experiments confirm the deformability of the MMG in static external magnetic fields[29,30] as predicted by simulations.[31,32] The experimental deformations subceded the theoretical predictions. That partially originates from a non-reactive polymer core, because the core is MNP free.[33] The reported core/shell structure[17,34,35] was altered to a homogeneous distribution of MNPs.[33] Recent research shows that the NP distribution relates to the total electric charge,[31] the cross-linker distribution,[33] and

[a] *Department of Physics, Soft Matter at Interfaces, Technical University Darmstadt, Hochschulstraße 8, 64287 Darmstadt, Germany. E-mail: klitzing@smi.tu-darmstadt.de; Tel: +49 6151 16-24506*
[b] *Faculty of Physics and Center for Nanointegration Duisburg-Essen (CENIDE), University of Duisburg-Essen, Lotharstr. 1, 47057 Duisburg, Germany*
[c] *Institute of Physical Chemistry, Hamburg University, Grindelallee 117, 20146 Hamburg, Germany*

† Electronic supplementary information (ESI) available. See DOI: 10.1039/d1sm01597d

the degree of swelling.[36] Various realizations are reported on how the polymer matrix binds with the MNPs. For example the MNPs bind covalently to the polymer network[37,38] or non-covalently by embedding MNPs into brushes[39] or microgels.[31,33,40] Most studies measure the deformability[29,31] or separability[31,41,42] of the magnetic microgels. To the best of our knowledge, the literature misses experimental studies on the interaction strength between MNPs and the microgel network investigated with magnetic experiments. Campanella *et al.* showed the influence of hydrophobic MNP on the dynamics of hydrogels.[43] As Campanella *et al.* pointed out it is of high interest to distinguish between mobile and trapped MNP. The interaction is a crucial parameter to design multi responsive microgels. Recently, *e.g.* Hess *et al.* analyzed nanoparticle motion affected by surrounding polymer networks in terms of effective quantities utilizing the Gemant–DiMarzio–Bishop model.[44] Here the interaction strength between the MNP and the PNIPAM microgel matrix is studied in dependence of the temperature. Forces acting upon the MNPs are transferred to the polymer matrix or *vice versa*. This transfer depends on the interaction strength, which can be probed by studying the Brownian relaxation of the embedded magnetic nanoparticles. The relaxation frequency is influenced by the viscosity of the surrounding medium. Spatial constrains (the polymer chains) increase the Brownian relaxation time. Using thermoresponsive magnetic microgels based on PNIPAM, the spatial constrains can be controlled by changing the temperature. Therefore, the interaction strength between MNPs and the polymer network can be controlled.

We report a measure for the interaction strength between MNPs and the surrounding polymer network, by measuring the partially quenched magnetic Brownian relaxation of the MNPs. Furthermore, this work shows the influence of a hydrophobic co-monomer (allyl mercaptan) on the microgel properties and the distribution of MNPs inside the microgel. The microgel properties were measured with dynamic light scattering and electrophoretic mobility. Magnetometry and AC susceptibility studies were performed and the interaction between MNPs and polymer matrix was derived.

2 Experimental section

2.1 Materials and preparation

2.1.1 Materials. The microgels were synthesized with *N*-isopropylacrylamide (NIPAM), *N*,*N*′-methylene-bis(acrylamide)-(BIS), allylamine (AA), allyl mercaptan (AM), Ellman reagent and 2,2′-azobis(2-amidinopropane) dihydrochloride (AAPH) purchased from Sigma-Aldrich. The MNP were synthesized with iron(II)chloride (water free) purchased from Merck, cobalt(II)-chloride hexahydrate and iron nitrate nonahydrate from Sigma-Aldrich, nitric acid, citric acid and sodium hydroxide from Güssing, and disodiumcitrate from Honeywell. The chemicals were used as purchased, without further purification. The water for the experiments was purified with a Millipore Milli-Q device. The Milli-Q water had a resistance of 18.1 MΩ (@25 °C). The gold wafers were purchased from Sigma-Aldrich and cleaned with toluene and acetone in a ultrasonic bath for 5 min.

2.1.2 Magnetic nanoparticle synthesis. The cobalt-ferrite nanoparticles were synthesized by precipitation in a boiling solution of 1 M sodium hydroxide. Cobalt(II)-chloride hexahydrate and iron(III)-chloride were added to the sodium hydroxide solution. The MNPs were washed with water and transferred into a solution of 2 M nitric acid and 0.35 M iron(III)-nitrate. The solution was stirred at 80 °C for 20 min. The MNPs were then dialyzed against sodium citrate and citric acid for one week and were later dispersed in water with sodium hydroxide at a final pH of 8. The MNPs had a core diameter d_c of 12.2 ± 3.2 nm. The diluted MNPs had an electrophoretic mobility (EM) of −4.03 μm cm V^{-1} s^{-1} and a zeta potential of −38 mV. Fig. S1 (ESI†) shows the TEM image of the MNPs.

2.1.3 Microgel synthesis. The polymerization was performed in a double-walled glass reactor to maintain a steady temperature. The temperature was controlled with a thermostat with an accuracy of ±0.1 K. The reactor holds up to 300 mL and was equipped with ground joints for the feeding syringe, nitrogen flushing, reflux condenser and glass stirring rod.[33]

The microgels were polymerized with a positive charged initiator (AAPH) and a positive charged co-monomer allylamine *via* surfactant-free precipitation polymerization introduced by Pelton and Chibante.[45] The positively charged microgel was designed to increase the interaction strength between the negatively charged MNPs and the polymer matrix. A homogeneous distribution of MNPs was achieved with homogeneous cross-linked microgels, synthesized by the feeding method, as described elsewhere[33] and similar to ref. 46. The reactor was preloaded with 120 mL Milli-Q water. That water was heated to 80 °C and degased with nitrogen for 1 hour. The reactants were weigthed and solved in 40 mL Milli-Q water. This solution was also degased with nitrogen for 1 hour. The AA was added after degasing to prevent evaporation. The reactant solution was split in two and filled into syringes. AAPH (67.5 mg) was added into the reactor to start the formation of radicals. The reactants were fed into the reactor using a syringe pump with a feeding speed of 2 mL min^{-1}. This feeding method was designed to counteract the faster consumption rate of the crosslinker BIS compared to the monomer NIPAM, yielding a homogeneous cross-linker distribution across the microgels.[33,46]

1 mL of AM was added to one of the microgel batches, with a concentration of β = 58 mg mL^{-1} in the last minute of the reaction. The polymerizations were performed one after another, starting with the microgel without AM. The reactor was cleaned in between the polymerizations. The feeding reaction was stopped after 10 min by rapid cooling. The microgels were cleaned by dialysis for 7 days and freeze-dried afterwards. Both microgels were polymerized with 3 mol% BIS and 3 mol% AA. Microgel 1 (MG1) was synthesized without AM and microgel 2 (MG2) was synthesized with AM. The amount of reactants used for both microgels was 20 mmol in a total reaction volume of 150 mL.

2.1.4 Magnetic microgel preparation. The magnetic microgels were prepared by loading the microgels with MNPs. For this purpose, the freeze-dried microgels were redispersed

in water for 24 h at a stock concentration of β = 0.5 wt% the measured pH was 7 (no salt, acid or base was added). The MNP stock suspension had a concentration of β = 5.8 wt%. Both dispersions have been placed in the ultrasonic bath for 10 min. The magnetic microgels were prepared by mixing 50 mL of microgel dispersion with 4.3 mL MNP suspension and water to a total volume of 1 mL. The following cleaning process was used to remove free MNPs from the dispersion. The mixture was vortexed at 1500 rpm for 30 min. Afterwards the mixture was centrifuged at 2000 rpm for 30 min. The supernatant was removed and the precipitant was redispersed in water. The cleaning process was repeated three times to remove free MNPs. The magnetic microgel dispersion had a measured pH of 7 and a measured concentration of about 0.06 wt% of magnetic microgels. The concentration was calculated from the measured densities. The resulting magnetic microgels were MMG1 from MG1 (without AM) and MMG2 from MG2 (with AM).

2.2 Methods

2.2.1 Dynamic light scattering (DLS). The hydrodynamic radii r_H of the microgels and magnetic microgels were measured with dynamic light scattering (DLS). The DLS setup was purchased from LS-Instruments consisting of a solid-state laser (λ = 660 nm, up to 100 mW), two avalanche photo diodes, hardware correlator, goniometer and temperature adjustable sample chamber of an index matching bath filled with decahydronaphthalene (to match the refractive index of glass). The measurement angle was varied between 30° and 120°. The temperature was adjusted between 15 °C and 50 °C with ΔT = 0.1 K. The hardware correlator processed data were fitted with a self-written script based on the cumulant fit procedure. The samples were sufficiently diluted so that no multiple particle scattering occurs and particle–particle interaction can be neglected. The swelling ratio is defined as $\alpha = \frac{r_H^3(20\ ^\circ\mathrm{C})}{r_H^3(50\ ^\circ\mathrm{C})}$. The mesh sizes inside the microgels were estimated from the swelling ratio. Canal *et al.* showed the relation between the mesh size and the amount of cross-linker[47] is:[48]

$$\zeta = l \times \left(\frac{2M_c}{M}\right)^{1/2} C_N^{1/2} Q^{1/3} \quad (1)$$

l is the length of a C–C bond (l = 0.154 nm), M is the average molar mass of the monomers, C_N is the characteristic ratio (here 6.9)[49], M_c is the molar mass between two cross-linkers ($M_c = n_{NIPAM} \times M_{NIPAM}/n_{BIS} + M_{BIS}$) and Q the degree of swelling.

2.2.2 Electrophoretic mobility. The electrophoretic mobility (EM) was measured with a Malvern Nano-ZS. The laser had a wavelength of 633 nm with 4 mW, with the backscattered light being measured at 173°. The zeta potential of the MNPs was calculated from the EM *via* the Hückel approximation.

2.2.3 UV/vis spectrometer. The long term stability of the magnetic microgel dispersions was analyzed with UV/vis absorption spectroscopy. A UV/vis spectrometer Lambda 650 from PerkinElmer was used. UV/vis absorption spectra were measured from 350 nm to 800 nm once per hour. The spectra were measured at 20 °C once and every hour at 50 °C over a period of 2 days and afterwards again at 20 °C. The presence of –thiol groups inside the MGs was measured at 415 nm with the addition of Ellman reagent.

2.2.4 Transmission electron microscopy (TEM). The MNPs and magnetic microgels were imaged with a FEI CM20 transmission electron microscope (FEI, Eindhoven, The Netherlands) with a LaB_6 cathode. The acceleration voltage was set to 200 kV. The sample was mounted with a Gatan double tilt holder. The samples were prepared on a copper grid covered with a carbon film (300 mesh, Science Service, Munich, Germany), by putting a 5 mL drop of the dispersion (β = 0.05 wt%) for 1 min onto the grid. The excess dispersion was removed afterwards. The samples were dried at room temperature (22 °C‡) in a dust free environment over night. While the images of the MNPs had a resolution of 0.4 nm per pixel, the images made on the MMGs had a resolution of 4 nm per pixel. The pure microgels have been stained with vanadium oxide to increase the contrast.

2.2.5 Magnetometry and AC-susceptometry. The magnetization- as well as the AC-susceptibility measurements were performed using a Quantum Design MPMS-5S SQUID magnetometer with an integrated AC option. About 50 μL of the MMG dispersions were placed into a PCR tube, the lid of which was then melted shut to provide a gas-tight holding for the MMG sample material, required due to the helium underpressure atmosphere in the SQUID sample chamber. Individual samples of the same batch were used for magnetometry and AC-susceptibility to circumvent aging effects or permanent changes inflicted during one measurement protocol affecting the other. For temperature-dependent magnetization measurements the standard zero-field-cooled/field-cooled (ZFC-FC) protocol was employed, using a magnetic field of 10 mT and heating/cooling rates of 2 K min^{-1}. In short the sample is cooled down without an external field. The ZFC curve is then recorded while heating the sample. Afterwards the sample is cooled down in presence of an external magnetic field (FC). AC-susceptometry measurements were performed upon rising temperature, held constant at each set point, with temperature steps ΔT of 0.5–5 K at frequencies between 0.1 Hz and 1500 Hz, using 8 equidistant frequency steps per order of magnitude and an AC-field of 0.1 mT.

3 Results and discussion

3.1 Structure of (magnetic) microgels

3.1.1 Dynamic light scattering. The microgels and magnetic microgels show the typical expected temperature responsive behavior. The DLS data are shown in Fig. 1(a). A more detailed view of the first heating/cooling cycle is shown in Fig. S2 (ESI†) for the MGs and in Fig. S3 (ESI†) for the MMGs.

‡ All temperatures are calculated to even numbers in °C to simplify the text for readability.

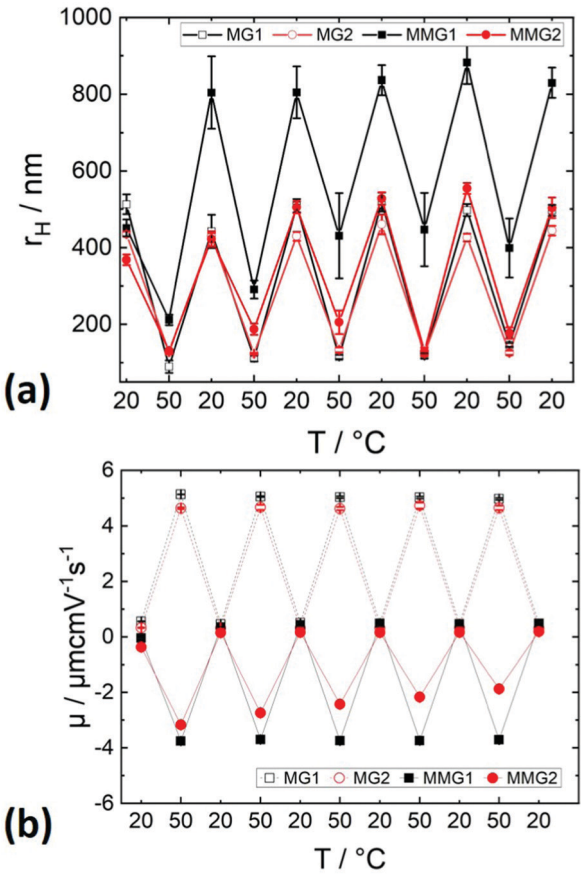

Fig. 1 (a) Hydrodynamic radii and (b) the electrophoretic mobility plotted over several heating/cooling cycles. The microgels (MG1 and MG2) are plotted with open symbols and the magnetic microgels (MMG1 and MMG2) are plotted with closed symbols.

The VPTT of MG1 and MG2 is 31 ± 1 °C and 28 ± 1 °C respectively. The VPTT for MG1 is in good agreement with the literature, while for MG2 the VPTT is lower. This indicates an influence of the AM on the microgel structure. For MG1 the hydrodynamic radius decreases from an average of 495 nm to an average of 115 nm by increasing the temperature from 20 °C to 50 °C and for MG2 from 437 nm to 126 nm. The hydrodynamic radius stays constant above a temperature of 40 °C. The VPTT for MMG1 is 32.2 °C and for MMG2 30.9 °C. The higher VPTT for MMG compared to the MG may be a consequence of the MNP embedding, which increase the energy needed to break the hydrogen bonds inside the network structure or indicates a steric reorientation. Both microgels show a similar size in the shrunken state, thus indicating the same amount of consumed monomers, as expected due to the identical syntheses until the ninth minute. That is in good agreement with the literature as already small deviations in the microgel composition results in different sizes in the shrunken state.[31,50,51] Small differences of the size in the shrunken state are expected due to the addition of AM to MG2 in the last synthesis minute (between 9th and 10th minute). This difference becomes more prominent in the swollen state where MG2 is smaller than MG1. The size difference in the swollen state and the broadened VPTT-region indicates that the microgel structure is different. These differences originate from the addition of AM in the 9th minute of the polymerization of MG2. The presence of -thiol groups was determined with absorption measurements at 415 nm after the addition of Ellman reagent.

The swelling ratio of the first temperature cycle for MMG1 and MMG2 is smaller than for the corresponding microgels MG1 and MG2 (compare Fig. S2 and S3 (ESI†), supporting information). The swelling ratio of the MMGs is larger for all subsequent cycles. The larger size for MMG compared to the respective MG is well known from literature and originates from the Gibbs-Donnan effect.[31,33] The change in size after the first heating/cooling cycle is more pronounced for MMG1 compared to MMG2. This rearranging of the magnetic microgel structure is well known for microgels.[31,33] The microgel sizes above and below the VPTT are almost constant for both MMGs after the first cycle. This shows that the re-arrangement of the internal microgel structure as well as the MNP position became stable after an initial shrinking/swelling cycle. Fig. 1 shows the hydrodynamic radius of the microgels (open symbols) and magnetic microgels (closed symbols) at two different temperatures (20 °C and 50 °C) for several cycles. This graph shows that the shrinking/swelling is completely reversible and reproducible over several cycles.

The swelling ratio is α = 86.3 for MG1, α = 10.1 for MMG1 and α = 41.7 for MG2, α = 28.0 for MMG2. With eqn (1) the mesh sizes for the microgel are calculated to ζ_{MG1} = 14.5 nm and ζ_{MG2} = 11.4 nm. The calculated mesh size is the lower limit, because not all water molecules might be expelled from the microgel in the collapsed state. Additionally, the diameter of the embedded MNPs is also a lower limit of the mesh size, as the MNPs are capable to be embedded in the microgels. MMG2 shows that the MNP are embedded into the MG2, therefore, the mesh size is above 12.2 nm. Table 1 shows the hydrodynamic radii, the swelling ratio and the estimated mesh size of the samples. The MNPs and the mesh size are of the same length scale *i.e.* the collapsed microgel matrix influences the MNPs more strongly.

3.1.2 Electrophoretic mobility. Fig. 1(b) shows the electrophoretic mobility (EM) of MG1 and MG2 (open symbols) and MMG1 and MMG2 (closed symbols) for several temperature cycles (between 20 °C and 50 °C). Both microgels show a positive charge. With rising temperature the surface charge density increases and therefore, also the electrophoretic mobility. The change of electrophoretic mobility is reversible as it is shown for several heating/cooling cycles. Table 1 shows the

Table 1 Characteristic measurements of the microgels, mean hydrodynamic radii r_H and the swelling ratio α and mean electrophoretic mobility μ (@20 °C and @50 °C)

Sample	$r_H^{20°C}$/nm	$r_H^{50°C}$/nm	α	$\mu^{20°C}$/ μm cm V^{-1} s^{-1}	$\mu^{50°C}$/ μm cm V^{-1} s^{-1}
MG1	495	115	86.3	0.47	5.04
MG2	437	126	41.7	0.32	4.66
MMG1	767	355	10.1	0.44	−3.73
MMG2	491	161	28.0	0.16	−2.47

average electrophoretic mobility at 20 °C and 50 °C. The MGs are positively charged due to the positively charged reactants in the synthesis. The literature shows that with increasing AA concentration during synthesis leads to an increase in microgel charge, which is a hint of incorporation of AA into the polymer network.[31] The distribution of AA is unknown, but can be estimated. For the feeding method two extreme cases can be considered. The first case where the consumption rate of AA is slower. Here the AA would accumulate over time in the reaction and the concentration of available AA that would be build in increases. The second case would be a faster consumption of AA that results in a deficiency of AA and the build in process is dominated by the feeding speed. In a former study the first case could be ruled out due to the distribution of MNP.[33] A core/shell structure for AA with a higher amount of AA in the shell would hinder the migration of MNP into the microgel core, that could not be observed. This indicates that the consumption of AA is either similar to the cross-linker consumption or faster.

The magnetic microgels exhibit a reduced electrophoretic mobility compared to the corresponding pure microgels, since the positive charges of the microgel are partially neutralized by the negatively charged MNPs. For both magnetic microgels the electrophoretic mobility becomes negative at 50 °C, where the magnetic microgels exhibit a charge reversal. The change in EM is reversible and reproducible. For MMG2 the EM seems to decrease linearly with an increasing number of cycles. A detachment of the MNPs is not expected as since the potential and size is reversible over several heating and cooling cycles. The charge reversal observed by crossing the VPTT can be explained by the decreased surface area but constant number of charges provided by the MNPs. Combining these findings with the DLS measurements it can be concluded that the MMGs retain their gel like properties after being loaded with MNPs.

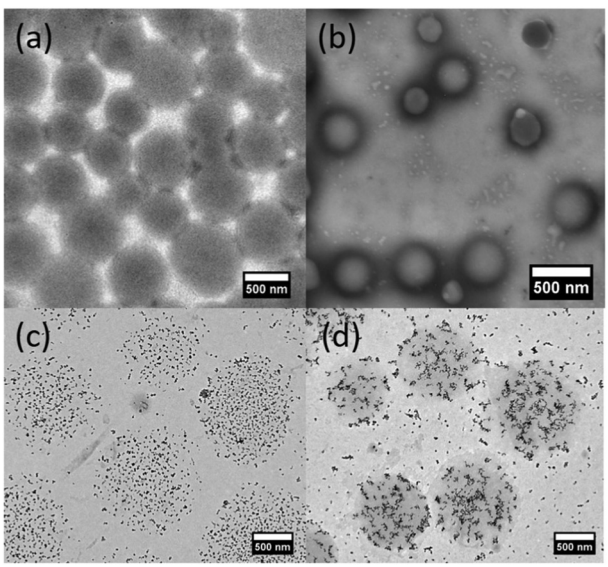

Fig. 2 TEM images of the microgels and magnetic microgels: (a) MG1, (b) MG2, (c) MMG1 and (d) MMG2.

3.1.3 Transmission electron microscopy. Fig. 2 shows the TEM images of the pure microgels in part (a and b) and for the magnetic microgels in part (c and d). The microgels themselves are not visible due to the low electron density and the resulting low TEM contrast. The pure microgels are stained with vanadium oxide to increase the contrast. Both microgels show a constant gray value over the whole microgel particle, with some higher accumulation of vanadium oxide on the particle surface. The visible microgels are spherical. The magnetic microgels show different distributions of MNPs: for MMG1 the MNPs are well separated, with only small clusters being present, while for MMG2 the MNPs are arranged in small clusters or short chains, respectively. The different MNP arrangement is expected to originate from the AM in MG2 (MMG2), because MG1 shows similar MNP distribution as reported in the literature.[31,33] AM reduces the microgel charge and is hydrophobic. This may lead to an increased MNP aggregation.

3.2 Magnetic properties

3.2.1 Magnetometry. In Fig. 3 the magnetization of the magnetic microgels is plotted over the temperature. Both samples show qualitatively similar behavior, with the overall magnetization of MMG2 being two to three times smaller

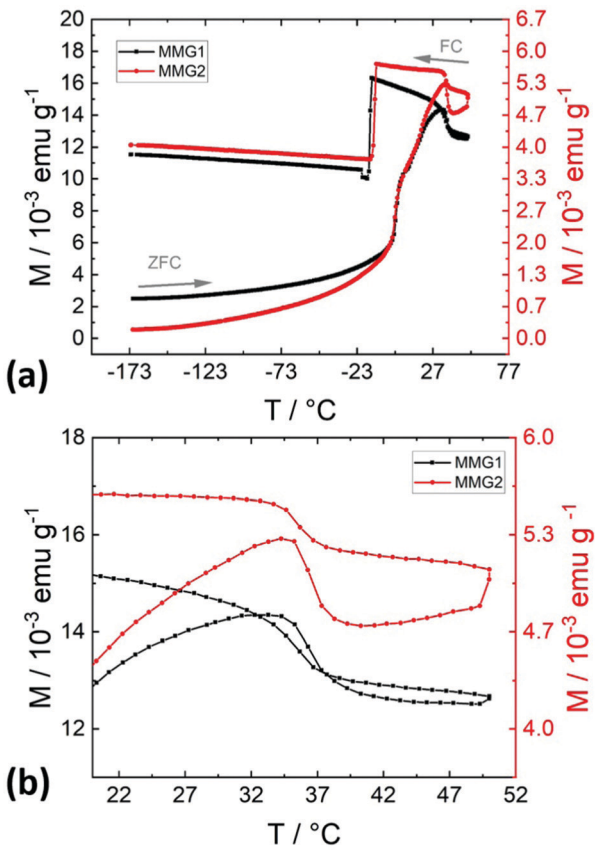

Fig. 3 ZFC-FC magnetization curves of MMG1 (black) and MMG2 (red) recorded from −173 to 50 °C in an external magnetic field of 10 mT. In (a) the complete temperature range is plotted while in (b) the temperature range is focused around the VPTT from 20 to 50 °C.

compared to MMG1. Minor differences in the concentration of magnetic material in the different microgel samples are possible. The difference in the maximum magnetization reached in the ZFC-FC measurements can most likely be explained by a different number of magnetic nanoparticles reaching the completely superparamagnetic state. Therefore, the difference in amplitude of $m_{ZFC\text{-}FC}$ may be a result of the difference in MNP structure inside the microgels. The lower amplitude for MMG2 compared to MMG1 could indicate the presence of agglomerates, also observed in the TEM images, as they seem to be more resilient to the applied magnetic field. In the magnetic agglomerates the resulting magnetic moment is reduced due to partial cancellation of their magnetic moments. In the temperature range between −173 °C and about 0 °C the splitting between the ZFC- and FC magnetization branch (m_{ZFC}, m_{FC}) decreases moderately. This reflects the minor fraction of small $CoFe_2O_4$ nanoparticles experiencing sufficiently fast Néel-type superparamagnetic relaxation at such low temperatures, thus allowing the dynamic realignment of the individual particle's magnetic moment. A first fast increase in the ZFC-magnetization close to the water melting point is explained by the onset of Brownian particle motion. This permits the partial alignment of larger particles still blocked in terms of Néel relaxation along field direction. A second, less pronounced increase in m_{ZFC} is visible at higher temperatures, possibly originating from faster microgel particle rotation close to the VPTT, crossing the timescale of the magnetization measurement. Sample MMG1 shows no splitting of the ZFC- and FC-branch above the VPTT of the microgels, indicating that a complete superparamagnetic state is reached with no further change in particle dynamics. The magnetization curves of MMG2 on the other hand are split up to the maximum measurement temperature, revealing an ongoing magnetic relaxation even at temperatures clearly above the VPTT, as also visible at 40 °C when switching from heating to cooling by the time-dependent increase in magnetization. The latter indicates a fraction of magnetic nanoparticles or microgel particles, respectively, which are still magnetically blocked on the timescale of the experiment. As is later on illustrated in detail in terms of AC-susceptometry, the different behavior close to the VPTT could be explained by a higher mobility of MNPs in the wider PNIPAM microgel meshes in MMG1 compared to MMG2. That would be in agreement with the moderately higher water uptake of MMG1 as pointed out by its higher swelling ratio. This is further supported by the TEM images showing lower inclination for clusters to manifest in sample MMG1 as compared to MMG2. On the contrary, MNPs in MMG2 only display completely superparamagnetic behavior in case of sufficiently fast microgel particle rotation. This can be assumed, as their trapped state in the gel meshes should not allow spatial reorientation of individual magnetic nanoparticles and small MNP clusters. Fig. 3(b) shows a close-up of the high-temperature region for both samples. A rapid decrease in m_{ZFC} is observed above 34 °C for both samples, expected to correspond to the VPTT of the MMGs, both being slightly higher as compared to DLS measurements. The higher VPTT found here in magnetization measurements relative to those from DLS may be a result of the different experimental setup and measurement principles. In the FC branch of the measurement, both samples display a spontaneous drop in m_{FC} at about −18 °C, where the sample is undergoing the transition from the supercooled liquid to the solid state. This phenomenon has recently been discussed for ferrofluids based on polyethylene (PEG)-solutions. It was assigned to torques acting on individual nanoparticles during the phase separation (crystallization) process. These may originate either from enhanced interparticular magnetic interaction within the remaining fluid volume or mechanical or hydrodynamic interaction with forming ice-crystal structures.[52]

3.2.2 Temperature dependent AC-susceptibility. To gather closer information on temperature dependent relaxation dynamics of individual MNPs as well as of the microgel particles, magnetic AC-susceptometry measurements were performed at temperatures of 0–50 °C. Results are shown exemplarily in Fig. 4 for 20 °C.

To ensure easier comparability of particle dynamics in both microgel systems, the magnetic susceptibility is normalized with respect to $\chi'(0)$ from modeling discussed below. A dominant peak occurs in the imaginary part of the magnetic susceptibility χ'' close to 1 Hz, being more pronounced for MMG2 than for MMG1. A minor broad susceptibility component stretches up to maximum attainable frequencies of about 1.5 kHz, showing higher intensity and an increase upon rising frequency for sample MMG1. Solid lines in Fig. 4 stem from

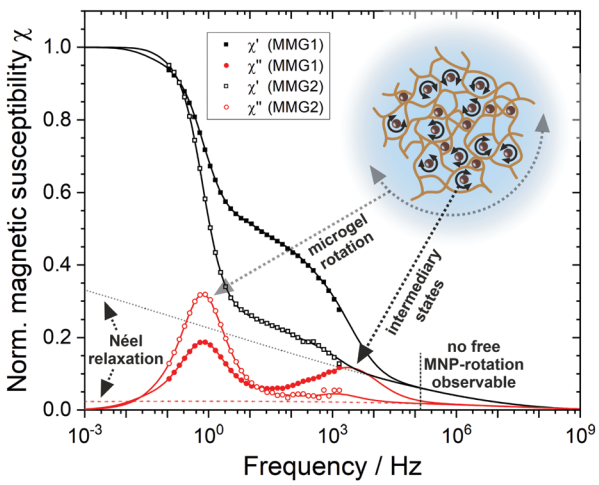

Fig. 4 Magnetic susceptibilities χ of MMG1 (filled) and MMG2 (open symbols) recorded at 20 °C. Data points were theoretically reproduced *via* a phenomenological model as described in the text (solid lines). Frequency regions are labeled with regard to their predominant relaxation mechanism as illustrated by the schematic structure of a microgel particle, showing contributions of free as well as trapped magnetic nanoparticles: Microgel rotation (~1 Hz), intermediary states (1 Hz < f < 100 kHz), free nanoparticle rotation at *ca.* 120 kHz (not observed), and Néel relaxation (background signal, dominant at f > 100 kHz). For comparison, the Néel-type background signal (χ' grey dotted, χ'' red dashed) was added as simulated for identical relaxation parameters in absence of Brownian motion.

theoretical modeling of the experimental data points. Here, an extended Debye model was used, describing the distribution of Brownian- and Néel-type relaxation times (τ_B, τ_N) for an ensemble of magnetic nanoparticles, as defined in eqn (2) and (3):

$$\tau_B = \frac{4\pi\eta r_H^3}{k_B T} \quad (2)$$

$$\tau_N = \tau_0 \exp\left(\frac{K_{eff} V_c}{k_B T}\right) \quad (3)$$

Here k_BT is the thermal energy, η the dynamic viscosity of the solvent surrounding the MNPs, τ_0 a relaxation factor for magnetic nanoparticles often assumed to be in the range of 10^{-9} to 10^{-13} s[53], which is fixed to τ_0 = 1 ps, K_{eff} the effective magnetic anisotropy energy density and V_c the particle core volume. The utilized model is similar to that described by Hankiewicz neé Fischer *et al.*[54] In the present study a log-normal distribution is used with core diameters of d_C = 12.2 ± 3.2 nm, as determined for the spherical cobalt ferrite (CFO) NPs without citrate shell *via* TEM analysis. However, up to this point we lack an adequate theoretical model to describe the complex AC-susceptibility signal structure of MNPs experiencing varying degrees of confinement. Depending on the microgel mesh size, one would expect the MNPs *e.g.* to perform free rotation in wider meshes and dampened or decelerated rotation with decreasing mesh size, due to repeated contact with the surrounding polymer strings. When trapped in even narrower spaces, *i.e.* meshes of minimum size close to the MNP diameter or in the collapsed PNIPAM microgel state, spatial realignment of the particles should no longer be possible.

Therefore, the following phenomenological model is applied to reproduce the Brownian contributions to the magnetic susceptibility signal: To describe different degrees of particle confinement, core–shell nanoparticles are modeled, with core diameters as described above and a free distribution of non-magnetic shell thicknesses. The particle is assumed to move through water, with the temperature-dependent variation in water viscosity being considered by using literature values of $\eta_{H2O}(T)$.[55] Here a minimum total particle hydrodynamic diameter d_H of 15 nm (CFO-core plus citrate coating) represents contributions of free MNP rotation in water. Higher effective hydrodynamic diameters correspond to slower Brownian rotation, representing higher degrees of spatial particle confinement, where the friction acting on the rotating MNPs is increased. The maximum values of d_H are thus expected for narrow microgel pores, where trapped MNPs can only add to the magnetic susceptibility signal by the rotation of the whole microgel particle they are embedded in. The upper end of the distribution $P(d_{eff})$ thereby labels the microgel particle diameter. Alternatively, as discussed in more detail below, the simulation results can be understood as distributions of effective viscosities of the medium the MNPs are moving in. For that purpose a fixed value of d_H = 15 nm is assumed, corresponding to identical values of $\eta \cdot {d_H}^3$, *i.e.* identical distributions of relaxation times. The latter interpretation may be more intuitive to describe hindered MNP motion when coming from soft matter dynamics. As can be seen below, this model can successfully reproduce experimental AC-susceptometry data, while being limited to the above-mentioned effective parameters, as interactions between MNPs and the local environment are not considered explicitly.

The magnetic nanoparticles which are completely mechanically blocked by their surrounding only contribute to the susceptibility *via* rotation of the whole microgel particle. The low-frequency peak in χ'' in Fig. 4 at about 1 Hz is assigned to microgel particle rotation using eqn (1). Therefore, it will contribute at a rotation frequency corresponding to the hydrodynamic microgel diameter depending on the specific sample and measurement temperature. On the contrary, free rotation of the MNPs in large microgel pores assuming a hydrodynamic diameter d_H of about 15 nm and a viscosity of water of η(20 °C) ≈ 1 mPa s, would translate to a Brownian rotation frequency of about 120 kHz. This frequency is not directly observable in the attainable frequency range with the used SQUID setup. However, the absence of free MNPs can be inferred for both samples from the low value of χ' at about 1 kHz. Contributions in the intermediate frequency range of about 1 Hz $< f <$ 10^5 Hz are assigned to different states of particle confinement, which will be discussed in the next paragraph in detail, concerning temperature dependent variations in the MMG diameter.

In addition to Brownian contributions one can also analyze to some extent the frequency dependent Néel relaxation of the particles. This can be done based on the susceptograms taken above the VPTT at about 34 °C as shown in Fig. S4 (ESI†) in the supplementary. For sake of comparison, the pure Néel-type signal is also displayed in Fig. 4 (grey and red) as it would appear in absence of any Brownian processes. The signal is being calculated for identical parameters τ_0 and K_{eff} as in the complete model stated below. Information on the magnetic anisotropy energy barrier of the nanoparticles can be extracted from the remaining Néel susceptibility signal, stretching almost constantly over several orders in frequency due to the exponential dependence on the magnetic anisotropy energy. The ratio of χ' to χ'' in the measured frequency interval can be reproduced well using values of $\tau_0 \sim 10^{-12}$ s and $K_{eff} \sim 70$ kJ m^{-3}. As expected, the CFO MNPs display a relatively high magnetic anisotropy energy density compared to other ferrite nanoparticles. As illustrated by Cannas *et al.*, the magnetic anisotropy for such particles does not only depend on their size, but also strongly on the Co^{2+} site occupation in the spinel lattice, depending on the degree of structural order as well as on the particle preparation approach.[56]

By following this approach, the amplitude of the Néel relaxation background in the intermediate frequency region can be determined, which is necessary for the correct simulation of the dominant Brownian contribution. It becomes evident that the difference between MMG1 and MMG2 in partially free MNP motion assigned to susceptibility contributions in the range of *ca.* 1 kHz is even more pronounced. It can therefore be concluded that sample MMG1 has a much lower degree of constraint in mobility as analyzed below for varying temperatures.

Fig. 4 demonstrates that it is easier to identify the contributions of different relaxation mechanisms *via* the Debye-peak features in χ'' as compared to χ'. Therefore, Fig. 5 displays χ'' for MMG1 and MMG2 recorded upon rising temperature between 20 °C and 40 °C. This is providing information on effects on both primary Brownian contributions – microgel rotation and (partially) free MNP rotation – across the VPTT region. The signal does not change above 40 °C, (Fig. S4 and S5, ESI†). Fig. 5(a) depicts a shift of the low-frequency microgel rotation peak to higher frequencies for MMG1. The peak shift is in agreement with shorter Brownian rotation times being expected for decreasing microgel hydrodynamic diameters and viscosity when approaching the VPTT. The peak distinctly broadens at around 32 °C and is no longer visible as a distinguishable feature above the VPTT. In sample MMG1 the signal at about 1 kHz is assigned to partially dampened rotation of MNPs, located in microgel pores of intermediate size. The lack of further change in the susceptibility signal above 34 °C indicates Néel relaxation to be the primary magnetic relaxation process remaining above the VPTT. It is not completely clear, why no signal corresponding to the rotation of the ''collapsed'' MMGs is visible at/above the VPTT. Based on the radius as shown in Fig. S3 (ESI†), they should exhibit rotational frequencies of about 10^2 Hz. This frequency regime is well observable with the used measurement setup. A possible explanation is a higher tendency of the PNIPAM particles to agglomerate at these temperatures on the timescale of hours. That would be comparable to the timescale of the measurement of $\chi(f)$ at an individual temperature. Agglomeration may be favored due to the microgel particles' much higher effective density in the collapsed state. However, this could not be observed in time-dependent UV/vis absorption experiments on the MMGs. They were conducted at 20 °C as well as at 50 °C, showing no considerable decrease in sample stability at high temperatures. The measured integrated absorbance remained constant (0.288 ± 0.001 before heating and 0.297 ± 0.002 after heating).

In general, sample MMG2 exhibits similar behavior, showing a clear temperature dependent shift of the microgel rotation peak up to about 34 °C Fig. 5(b). Similar to MMG1 the AC-susceptibility measurements show a much lower signal contribution assigned to free or partially free MNPs. The different modes of particle mobility corresponding to specific degrees of spatial confinement are now analyzed in more detail:

Fig. 6 shows the distribution of effective diameter ($P(d_{\mathrm{eff}})$) and effective viscosity ($P(\eta_{\mathrm{eff}})$) for MMG1 in part (a) and MMG2 in part (b). The values d_{eff} and η_{eff} are calculated as described above in eqn (2), assuming constant values for $\eta_{\mathrm{eff}} \cdot d_{\mathrm{H}}{}^3 = \eta \cdot d_{\mathrm{eff}}{}^3$ for each given temperature. When discussing the thus extracted distributions, the limitations of this approach have to be kept

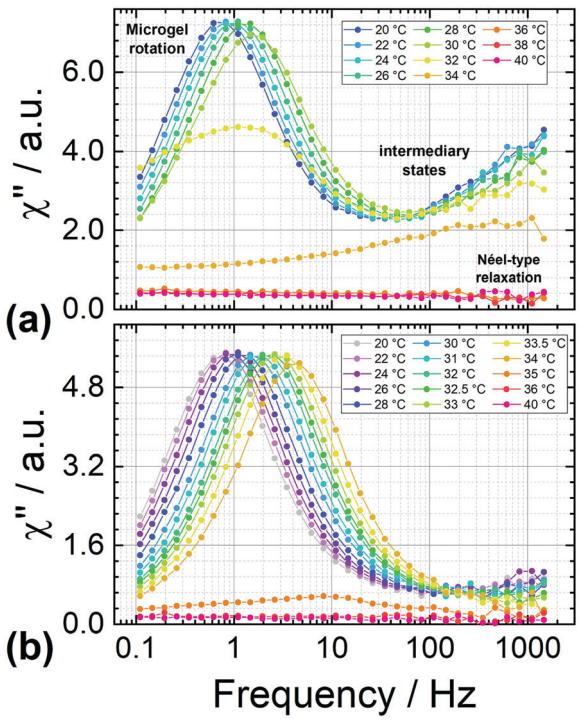

Fig. 5 Magnetic susceptibility data of MMG1 (a) and MMG2 (b) recorded at 20–40 °C. The enhanced high-frequency component in MMG1 is clearly visible, representing partially free MNP rotation, as well as the shift in the microgel rotation signal to higher frequencies when approaching the VPTT.

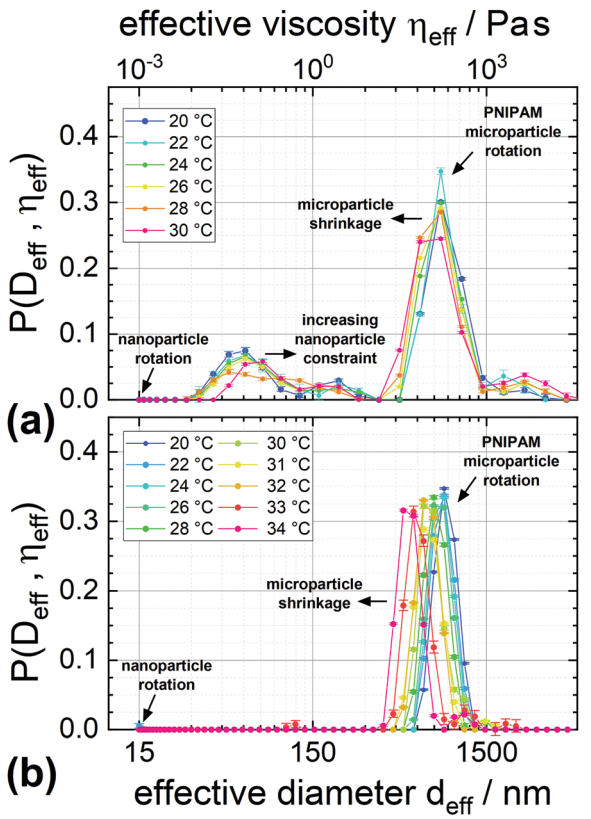

Fig. 6 Distributions of effective particle diameters and dynamics viscosities extracted from the modeling of rotational frequencies as determined from AC-susceptometry measurements of sample MMG1 (a) and MMG2 (b). Different signal distributions and noise levels have been evaluated and taken into account by choosing different numbers of sampling points of 30 (a) and 60 (b) in the d_{eff} – interval of 15 nm to 5000 nm, corresponding to MNP motion in dynamic viscosities of $\eta_{\mathrm{eff}} \approx 1$ mPa s to 4×10^4 Pa s.

in mind. For example the maximum and minimum frequencies reasonably usable by the utilized AC-susceptometer are *ca*. 1500 Hz and 0.1 Hz. These correspond to Brownian rotation timescales for effective particle diameters $d_{\mathrm{eff}} \approx$ 1600–65 nm (or, alternatively for 15 nm MNPs in a medium of $\eta_{\mathrm{eff}} \approx$ 0.08–10^3 Pa s).

While the contributions of small particles at high frequencies can be extrapolated to some extent from the trend in χ' in the high-frequency range close to 1 kHz, no information on particles much larger than 1600 nm is contained in the data. Also, the chosen number n of the distributions' sampling points as well as the smoothing factor λ applied to $P(d_{\mathrm{eff}})$ have some effect on the fine structure of the resulting distribution. However, as TEM and DLS results indicate that most of the microgels are of about 800 nm in diameter and since the low relative value of χ'(1.5 kHz) points to a negligible number of freely rotating MNPs assuming a continuous distribution $P(d_{\mathrm{eff}})$, these limitations do not obstruct the analysis in terms of microgel rotation and partially free (intermediary) MNP states.

All this considered, both microgel samples do not display high-frequency free rotation of individual MNPs, which could have been registered *via* enhanced values of χ'(1.5 kHz), despite being outside the directly accessible frequency range in a strict sense. This reveals the limited freedom for nanoparticle motion within the microgel pores even down to room temperature. Both samples display a similar position of the primary microgel peak, being slightly broader for MMG1. Here, a small contribution of larger microgels is indicated in $P(d_{\mathrm{eff}})$, which could explain the higher average hydrodynamic diameter determined *via* DLS for MMG1. At the same time, a considerable amount of intermediary diameters is present, assumed to represent partially constrained MNP rotation. This could presumably be explained by the higher average microgel diameter caused by moderately higher swelling compared to MMG2, leading to an expansion of the microgel pores and more space for the MNP rotation. MMG2 on the other hand (Fig. 6(b)), only exhibits the main microgel particle rotation, allowing for a more precise determination of temperature-dependent size variation: for MMG1 between 20 °C and 30 °C, the main signal shifts from about 900 nm to 700 nm and for MMG2 between 20 °C and 34 °C from 850 nm to 530 nm. These effective diameters are in good agreement with the general trends and for MMG2 also with absolute diameters from DLS, as shown in Fig. S3 (ESI†). A further dampening of (partially) free MNP dynamics in MMG2 may be introduced by slightly larger MNP structures as evident in TEM images. The size of MMG2 determined with ACS and DLS can be compared in more detail in Fig. S7 (ESI†), where the hydrodynamic radius is plotted over the temperature. The hydrodynamic radius $r_{\mathrm{H(ACS)}}$ is extracted by fitting a Gaussian profile to the effective diameter peaks. Both data sets display a similar trend in r_{H}, with differences in absolute numbers likely being connected to limitations of the data evaluation model regarding nanoparticle magnetic alignment in the microgel particles as illustrated below, defining the net magnetic moment of a microgel particle of given diameter.

One final observation for MMG1 is worth mentioning: The contribution representing partially limited MNP dynamics starts to decrease and shift to slightly higher values of d_{eff} at *ca*. 26–28 °C as visible in Fig. 6(a). When approaching the VPTT, the temperature-dependent increase in effective diameter (or effective viscosity, *vice versa*) accelerates. This could be ascribed to the reduction in microgel pore size, which accompanies the general shrinking of the microgel particle. This results in further constraint of the MNP rotational dynamics and is therefore shifting contributions into the microgel rotation signal, which previously were part of the intermediary states (partially constrained MNP dynamics). These findings add to the knowledge presented by Campanella *et al.* on the dynamic processes inside hydrogels influenced by the loading with MNP.[43]

While up to this point the extracted distributions of effective parameters were interpreted in terms of MNP mobility, a direct assignment to the number of MNPs exposed to a specific degree of confinement from those distributions is hindered due to uncertainties regarding the microgels' internal magnetic structure. With a core diameter of about 12 nm, the MNPs carry a considerable net magnetic moment (μ_{MNP}), leading to strong magnetic dipole interaction when being in close distance, explaining the minor tendency to form agglomerates even within the microgel particle structures (see Fig. 2). Therefore, it is unclear whether interparticle interaction will lead to some degree of alignment of easy magnetic directions, when embedding adjacent nanoparticles in the microgel or during the formation of minor MNP clusters. This essentially determines what fraction of MNP magnetic moments cancels each other out, and which remains to contribute to the microgel's net magnetic moment, *i.e.* to the magnetic susceptibility signal.

Assuming an array of N more or less aligned MNPs within a microgel particle, the latter will exhibit a net magnetic moment (μ_{MG}) approximately given by the sum of nanoparticle superspins ($\mu_{\mathrm{MG}} \sim N \cdot \mu_{\mathrm{MNP}}$). However, magnetic moments of N MNPs completely uncorrelated in terms of easy magnetic direction will partially cancel each other out. This will strongly reduce the microgel particle net magnetic moment $\left(\mu_{\mathrm{MG}} \sim \sqrt{N} \cdot \mu_{\mathrm{MNP}}\right)$, as is sometimes observed in magnetic nanoparticle agglomerates.[57,58] Thereby, the distribution extracted from the phenomenological model cannot be converted easily into a number distribution of MNPs in a specific state of confinement. For this, further knowledge about the microgels' magnetic structure including nanoparticle interaction effects and nanoparticle rheology would be required. A more sophisticated analysis taking these effects into account is planned after a more detailed study of the internal magnetic structure of the microgels *via* a combination of neutron scattering with remanent magnetometry experiments.

4 Summary

This work presents a way to measure the interaction strength between the MNPs and microgel chain network by using the damped magnetic relaxation induced by the MNP confinement

in the microgel meshes. Changing the hydrophobicity by AM incorporation leads to the formation of small MNP clusters. Comparing the small MNP cluster confinement with the single MNP confinement shows a higher dampening of the magnetic relaxation time. Larger particles have higher contact area to the polymer network and therefore a decreased particle mobility. The system is described utilizing a phenomenological model, which represents the Brownian and Néel relaxation. To some extent, both can be separated and interpreted independently. All together the MNPs are used to probe the inner structure of the microgels and the impact of the microgel mesh size on the magnetic properties and their interaction strength. Additionally, the MNP confinement can be controlled indirectly by varying the temperature and therefore the mesh size.

The TEM images of the MMGs show the influence of AM on the MNP distribution. The MNPs form small clusters inside the microgel in the presence of AM while without AM the MNPs are well separated. In addition, according to the lower swelling ratio the AM containing MG is assumed to have significantly smaller mesh sizes. The meshes of both MGs are of similar size as the MNPs. Therefore, the meshes present an enviromental confinement for the MNPs, and the collapse of the MGs has an effect on the MNP mobility. The majority of the MNPs are inside the microgels. One of the observed relaxation peaks ($\approx$1 Hz) shifts to higher frequency with increasing temperature, corresponding to smaller particle sizes, originating from the collapse of the MG by crossing the VPTT. The VPTT of the MMGs was observed with DLS, EM, ZFC-FC measurements and with AC-susceptibility. However, the reversible process could not be observed with AC-susceptibility. The Brownian relaxation peak vanishes above 34 °C and does not reappear upon cooling down. Until now the origin of this effect remains unknown as stability experiments with UV/vis absorption measurements and DLS do not show any aggregation. A second observed Brownian relaxation peak originates from the damped MNP relaxation of partially free MNP inside the meshes. These partially free MNPs are more confined in sample MMG2 (with AM) compared to MMG1 as they form small clusters in MMG2. The formation of MNP clusters is favored for the MG with AM (MMG2) as it appears to be more hydrophobic compared to its counterpart without AM (MMG1). The addition of AM also influences the swelling ratio of the MGs and their electrophoretic mobility. The overall consumed amount of reactants is similar as deviations would show up in the shrunken state.[31,50,51]

The findings open up various possible applications, such as tuneable drug delivery systems that change their magnetic response in dependence on the external environment. The combination of MNPs and microgels can be used for the creation of sensors, sensitive to multiple external stimuli. Additionally, the sensitivity of the device may be tuned or the sensor position adjusted within an external magnetic field. Furthermore, the interaction between MNPs and microgel network can be studied and may give a better understanding on polymer dynamic processes on a small scale. Overall the studied MMGs are a suitable starting point for further investigations on the interaction between MNP and MG matrix as well as a guideline for future applications with tunable MMGs.

Conflicts of interest

There are no conflicts to declare.

Acknowledgements

The authors gratefully acknowledge the financial support of the German Research Foundation (DFG) within the Priority Programme (SPP1681) ''Field controlled particle matrix interactions: Synthesis, multiscale modeling and application of magnetic hybrid materials'', in the projects WE 2623/7-3, FI 1235/2-1, FI 1235/2-2 and KL1165/18-1, as well as the CRC/TRR 247 (Project-ID 388390466, sub-project B02).

References

1 S. Talebian, M. Mehrali, N. Taebnia, C. P. Pennisi, F. B. Kadumudi, J. Foroughi, M. Hasany, M. Nikkhah, M. Akbari, G. Orive and A. Dolatshahi-Pirouz, *Adv. Sci.*, 2019, **6**, 1801664.
2 M. Malmsten, H. Bysell and P. Hansson, *Curr. Opin. Colloid Interface Sci.*, 2010, **15**, 435–444.
3 A. K. Yetisen, I. Naydenova, F. da Cruz Vasconcellos, J. Blyth and C. R. Lowe, *Chem. Rev.*, 2014, **114**, 10654–10696.
4 H. Nolte, S. John, O. Smidsrød and B. T. Stokke, *Carbohydr. Polym.*, 1992, **18**, 243–251.
5 A. Gandhi, A. Paul, S. O. Sen and K. K. Sen, *Asian J. Pharm. Sci.*, 2015, **10**, 99–107.
6 K. Jain, R. Vedarajan, M. Watanabe, M. Ishikiriyama and N. Matsumi, *Polym. Chem.*, 2015, **6**, 6819–6825.
7 M. Shibayama, S. Y. Mizutani and S. Nomura, *Macromolecules*, 1996, **29**, 2019–2024.
8 H. Senff and W. Richtering, *J. Chem. Phys.*, 1999, **111**, 1705–1711.
9 K. Kratz, T. Hellweg and W. Eimer, *Polymer*, 2001, **42**, 6631–6639.
10 S. Grobelny, C. H. Hofmann, M. Erlkamp, F. A. Plamper, W. Richtering and R. Winter, *Soft Matter*, 2013, **9**, 5862–5866.
11 M. Richter, *Doctoral thesis*, Technische Universität Berlin, Berlin, Germany, 2015.
12 V. E. Shashoua and R. G. Beaman, *J. Polym. Sci.*, 1958, **33**, 101–117.
13 F. W. Wang, C. W. Hsu and C. C. Hsieh, *ACS Appl. Mater. Interfaces*, 2019, **11**, 8591–8600.
14 A. Malfait, F. Coumes, D. Fournier, G. Cooke and P. Woisel, *Eur. Polym. J.*, 2015, **69**, 552–558.
15 T. Hoare and R. Pelton, *Macromolecules*, 2007, **40**, 670–678.
16 M. R. Islam, A. Ahiabu, X. Li and M. J. Serpe, *Sensors*, 2014, **14**, 8984–8995.

17 M. Lehmann, W. Tabaka, T. Möller, A. Oppermann, D. Wöll, D. Volodkin, S. Wellert and R. V. Klitzing, *Langmuir*, 2018, **34**, 3597–3603.
18 H. Lange, B. H. Juárez, A. Carl, M. Richter, N. G. Bastús, H. Weller, C. Thomsen, R. von Klitzing and A. Knorr, *Langmuir*, 2012, **28**, 8862–8866.
19 Z. Hedayatnasab, F. Abnisa and W. M. A. W. Daud, *Mater. Des.*, 2017, **123**, 174–196.
20 L. Schulz, W. Schirmacher, A. Omran, V. R. Shah, P. Böni, W. Petry and P. Müller-Buschbaum, *J. Phys.: Condens. Matter*, 2010, **22**, 346008.
21 K. Herman, M. E. Lang and A. Pich, *Nanoscale*, 2018, **10**, 3884–3892.
22 J. Zhang and R. D. Misra, *Acta Biomater.*, 2007, **3**, 838–850.
23 R. Gui and H. Jin, *RSC Adv.*, 2014, **4**, 2797–2806.
24 C. Dagallier, H. Dietsch, P. Schurtenberger and F. Scheffold, *Soft Matter*, 2010, **6**, 2174–2177.
25 C. Liu, J. Guo, W. Yang, J. Hu, C. Wang and S. Fu, *J. Mater. Chem.*, 2009, **19**, 4764–4770.
26 N. Nun, S. Hinrichs, M. A. Schroer, D. Sheyfer, G. Grübel and B. Fischer, *Gels*, 2017, **3**, 34.
27 J. E. Wong, A. Krishnakumar Gaharwar, D. Müller-Schulte, D. Bahadur and W. Richtering, *J. Magn. Magn. Mater.*, 2007, **311**, 219–223.
28 H. Y. Koo, S. T. Chang, W. S. Choi, J. H. Park, D. Y. Kim and O. D. Velev, *Chem. Mater.*, 2006, **18**, 3308–3313.
29 R. Weeber, S. Kantorovich and C. Holm, *Soft Matter*, 2012, **8**, 9923–9932.
30 A. Y. Zubarev and D. Y. Borin, *J. Magn. Magn. Mater.*, 2015, **377**, 373–377.
31 S. Backes, M. U. Witt, E. Roeben, L. Kuhrts, S. Aleed, A. M. Schmidt and R. von Klitzing, *J. Phys. Chem. B*, 2015, **119**, 12129–12137.
32 M. Bonini, S. Lenz, E. Falletta, F. Ridi, E. Carretti, E. Fratini, A. Wiedenmann and P. Baglioni, *Langmuir*, 2008, **24**, 12644–12650.
33 M. U. Witt, S. Hinrichs, N. Möller, S. Backes, B. Fischer and R. von Klitzing, *J. Phys. Chem. B*, 2019, **123**, 2405–2413.
34 K. Gawlitza, S. T. Turner, F. Polzer, S. Wellert, M. Karg, P. Mulvaney and R. von Klitzing, *Phys. Chem. Chem. Phys.*, 2013, **15**, 15623–15631.
35 A. P. Gelissen, A. Oppermann, T. Caumanns, P. Hebbeker, S. K. Turnhoff, R. Tiwari, S. Eisold, U. Simon, Y. Lu, J. Mayer, W. Richtering, A. Walther and D. Wöll, *Nano Lett.*, 2016, **16**, 7295–7301.
36 M. Bradley, N. Bruno and B. Vincent, *Langmuir*, 2005, **21**, 2750–2753.
37 Q. Wu, X. Wang, C. Liao, Q. Wei and Q. Wang, *Nanoscale*, 2015, **7**, 16578–16582.
38 X. Liang, Y. Deng, X. Pei, K. Zhai, K. Xu, Y. Tan, X. Gong and P. Wang, *Soft Matter*, 2017, **13**, 2654–2662.
39 F. Xu, J. H. Geiger, G. L. Baker and M. L. Bruening, *Langmuir*, 2011, **27**, 3106–3112.
40 A. Seyfoori, S. A. Seyyed Ebrahimi, E. Samiei and M. Akbari, *ACS Appl. Mater. Interfaces*, 2019, **11**, 24945–24958.
41 A. Khan, *Mater. Lett.*, 2008, **62**, 898–902.
42 A. Pich, S. Bhattacharya, Y. Lu, V. Boyko and H. J. P. Adler, *Langmuir*, 2004, **20**, 10706–10711.
43 A. Campanella, O. Holderer, K. N. Raftopoulos, C. M. Papadakis, M. P. Staropoli, M. S. Appavou, P. Müller-Buschbaum and H. Frielinghaus, *Soft Matter*, 2016, **12**, 3214–3225.
44 M. Hess, E. Roeben, A. Habicht, S. Seiffert and A. M. Schmidt, *Soft Matter*, 2019, **15**, 842–850.
45 R. H. Pelton and P. Chibante, *Colloids Surf.*, 1986, **20**, 247–256.
46 R. Acciaro, T. Gilányi and I. Varga, *Langmuir*, 2011, **27**, 7917–7925.
47 T. Canal and N. A. Peppas, *J. Biomed. Mater. Res.*, 1989, **23**, 1183–1193.
48 N. Adrus and M. Ulbricht, *React. Funct. Polym.*, 2013, **73**, 141–148.
49 N. A. Peppas, H. J. Moynihan and L. M. Lucht, *J. Biomed. Mater. Res.*, 1985, **19**, 397–411.
50 J. Thorne and M. Snowden, *Colloid Polym. Sci.*, 2011, **289**, 625–646.
51 A. Burmistrova, M. Richter, C. Uzum and R. V. Klitzing, *Colloid Polym. Sci.*, 2011, **289**, 613–624.
52 S. Webers, M. Hess, J. Landers, A. M. Schmidt and H. Wende, *ACS Appl. Polym. Mater.*, 2020, **2**, 2676–2685.
53 S. Mørup, E. Brok and C. Frandsen, *J. Nanomater.*, 2013, **2013**, 1–8.
54 B. Fischer, B. Huke, M. Lücke and R. Hempelmann, *J. Magn. Magn. Mater.*, 2005, **289**, 74–77.
55 J. Kestin, M. Sokolov and W. A. Wakeham, *J. Phys. Chem. Ref. Data*, 1978, **7**, 941–948.
56 C. Cannas, A. Musinu, G. Piccaluga, D. Fiorani, D. Peddis, H. K. Rasmussen and S. Mørup, *Int. J. Chem. Phys.*, 2006, **125**, 164714.
57 J. Landers, S. Salamon, H. Remmer, F. Ludwig and H. Wende, *ACS Appl. Mater. Interfaces*, 2018, **11**, 3160–3168.
58 F. Ludwig, A. Guillaume, M. Schilling, N. Frickel and A. M. Schmidt, *J. Appl. Phys.*, 2010, **108**, 033918.